Optik - International Journal for Light and Electron Optics 292 (2023) 171382

Contents lists available at ScienceDirect

Optik

journal homepage: www.elsevier.com/locate/ijleo

Dual-resonant-peak single-mode fiber surface plasmon resonance gas sensor with V-groove for methane detection

Xianli Li [a], Meiqi Liu [a], Wei Liu [a], Haihao Fu [a], Jianxin Wang [a], Lin Yang [a], Jingwei Lv [a], Qiang Liu [a], Paul K. Chu [b], Chao Liu [a,*]

[a] *School of Physics and Electronic Engineering, Northeast Petroleum University, Daqing 163318, China*
[b] *Department of Physics, Department of Materials Science & Engineering, and Department of Biomedical Engineering, City University of Hong Kong, Tat Chee Avenue, Kowloon, Hong Kong, China*

ARTICLE INFO

Keywords:
Single-mode fiber (SMF)
Surface plasmon resonance (SPR)
Methane sensing
Dual-band detection
Optical properties

ABSTRACT

Objective: The simple structure of single-mode fibers as a sensing platform circumvents the technical bottlenecks associated with manufacturing difficulties. Meanwhile, compared to photonic crystal fibers, they have lower manufacturing costs and can achieve similar performance to other types of fibers, providing greater possibilities for mass production. The V-groove in the SMF destroys the original symmetry of the fiber and renders the core mode energy leak controllable, consequently enhancing the sensitivity and confinement loss (CL) intensity of the core mode as well as the resolution. The composite nanolayer (gold gas-sensitive film) combines the advantages of both the materials and mutual gain to strengthen the detection ability and continuously outputs high-quality free electrons to promote mode coupling.
Methods: A dual-resonant-peak single-mode fiber (SMF) surface plasmon resonance (SPR) gas sensor with a V-groove is designed for the sensitive detection of methane and analyzed by the full-vector finite element method (FEM).
Results: By optimizing the structural parameters and polarization states, the SPR sensor can be operated in the concentration range between 0 % and 3.5 %, which can be spread across two transmission bands simultaneously with the maximum wavelength sensitivities being 12 nm/% and 8 nm/% and the corresponding resolution being 0.0083 % and 0.013 %, respectively. The tolerance of the structural parameters of the sensor is below 0.88 nm/μm to make manufacturing easier compared to conventional products. This sensor has good prospects and application potential in areas such as gas leakage diagnostics and environmental safety.

1. Introduction

Gas sensors are key components in detection systems used in medical diagnostics, environmental monitoring, public safety, and other applications [1,2]. For example, methane (CH_4) is a greenhouse gas contributing to global warming and also poses explosion risks in coal mines due to its flammable nature [9]. Therefore, accurate and sensitive detection of methane is crucial and common sensors include photonic crystal (PC) microcavity sensors, Fabry-Perot interference (FPI) microcavity sensors, and optical fiber grating sensors [3–5]. However, these sensors are prone to environmental interference, have low sensitivity, and are not easy for field

---

[*] Corresponding author.
E-mail address: msm-liu@126.com (C. Liu).

https://doi.org/10.1016/j.ijleo.2023.171382
Received 22 July 2023; Received in revised form 3 September 2023; Accepted 7 September 2023

commissioning [6,7].

Surface plasmon resonance (SPR) has advantages such as high sensitivity, fast detection speed, online real-time monitoring, and no need for special labeling [8] and several SPR-based sensing platforms of the prism and fiber types have been proposed [9]. Even though SPR is fairly well understood, the disadvantages of these systems are the high cost and bulky nature. As for the optical fiber sensing platforms, the single-mode fiber type and photonic crystal fiber type are the most attractive [10]. In particular, photonic crystal fibers (PCF) offer a flexible air hole layout, cutoff-free single-mode transmission, and large mode field area [11]. Yang et al. have designed a PCF methane sensor based on pattern interference with a sensitivity of 0.514 nm/% [12] and Liu et al. have proposed a PCF-SPR sensor with the polarization filtering capability that can achieve simultaneous measurement of hydrogen and methane with good sensitivities of − 0.19 nm/% and − 1.99 nm/% for hydrogen and methane [13]. Yang et al. have introduced a long-period photonic crystal fiber grating (PCF-LPG) methane sensor boasting a sensitivity of 1.078 nm/% [14] and Zhang et al. have demonstrated a sensor based on the cryptophane E infiltrated photonic crystal microcavity with a sensitivity of 1.67 nm/% [15]. However, in spite of the relatively flexible structural design and excellent transmission characteristics, there are manufacturing difficulties. In this regard, SMF has a simple structure and no air holes in the cladding and the production process is mature. SMF can thus be an excellent sensing medium [16,17].

Herein, an SPR methane sensor based on SMF is designed for high-sensitivity detection of methane. Compared to the same type of methane sensor, the performance of this sensor has been significantly improved [12,14]. The SMF incorporates a V-groove, the opening of which not only optimizes the transmission path, but also improves the momentum matching between the free electrons and photons. And a gold film and gas-sensing medium are formed on the V-groove to contact and detect methane. The V-groove achieves bidirectional coupling to amplify the SPR effect for sensitive monitoring of the changes in the gas refractive index around the SMF. The optimal structural parameters are derived by finite element analysis (FEM) with a wavelength sensitivity of 2–2.5 % methane concentration as the reference. The field coupling, light field distribution, structural parameter sensitivity, and resolution of the sensor are studied. The sensor can accurately detect methane at concentrations of 0–3.5 % across two transmission band intervals at the same time. The average wavelength sensitivity and resolution are 11.14 nm/% and 6.29 nm/% and 0.0083 % and 0.013 %, respectively, and the FOM at any concentration is below 10.36. The series output thresholds show a technical breakthrough and the sensor has immense potential in many areas such as environmental monitoring and mining exploration [18].

2. Structural design and numerical simulation

When light incidents from a light dense medium to a light sparse medium, total reflection occurs when the incident angle is greater than the critical angle of total reflection [19]. If there is a metal at the interfaces, the evanescent wave generated by total reflection will enter the metal and interact with free electrons to excite the surface plasmon wave (SPW) that propagates along the surface of the metal. The propagation constant K of the evanescent waves at the interface between the light dense medium and light sparse medium is determined by Eq. (1) [20].

$$K = \frac{\omega}{c}\sqrt{\varepsilon_{\text{core}}}\sin\theta_0 \tag{1}$$

where ω is the angular frequency of the light wave, c is the speed of light in vacuum, $\varepsilon_{\text{core}}$ is the dielectric constant of the core, and θ_0 is the angle of incidence. At the metal dielectric interface, when the wavelength of the incident light meets a specific requirement (resonance), the free electrons on the metal surface are excited to form the propagation constant K_{spw} of the surface plasma wave, which is determined by Eq. (2) [21].

$$K_{\text{SPW}} = \frac{\omega}{c}\sqrt{\frac{\varepsilon_{\text{m}}\varepsilon_{\text{s}}}{\varepsilon_{\text{m}}+\varepsilon_{\text{s}}}} \tag{2}$$

where ε_{m} is the dielectric constant of the metal, ε_{s} is the dielectric constant of the optically sparse medium, and ω is the angular frequency of the light wave.

If the propagation constants of the evanescent wave and SPW are equal, i.e. $K = K_{\text{spw}}$, the plasmonic wave on the metal surface will strongly couple with the evanescent wave, and most of the energy of the incident light will be converted into the energy of SPW. The energy of the reflected light suddenly drops and a resonant absorption peak appears in the reflection spectrum. The corresponding wavelength of the resonance peak is called the resonance wavelength [19]. The gold film on the surface of the SMF is extremely sensitive to variations in the refractive index of the surroundings, which directly affect mode coupling and can be reflected by the loss spectra of different analytes. The sensitivity of the plasmonic materials to changes in the gas concentration is low due to the wavelength drifts, and so a gas-sensitive film is introduced to improve the sensitivity. When a sensor coated with a film containing cryptane A is exposed to methane gas, small changes in the film RI result in a shift in the resonance wavelength. Based on the resonance wavelengths before and after the interaction with methane gas, the methane concentration can be obtained [22]. As the gas concentration changes, the refractive index changes as well to affect the mode coupling and produce a resonance wavelength shift for SPR sensing [23].

The essence of SPR is the energy exchange between the fundamental mode and metal plasmonic mode, manifested as the variation of fundamental mode confinement loss (CL) with wavelength as shown in Eq. (3) [24]:

$$CL = \frac{2\pi}{\lambda}\frac{20}{\ln(10)}\text{Im}\left(n_{\text{eff}}\right)/(\text{dB/cm}) \tag{3}$$

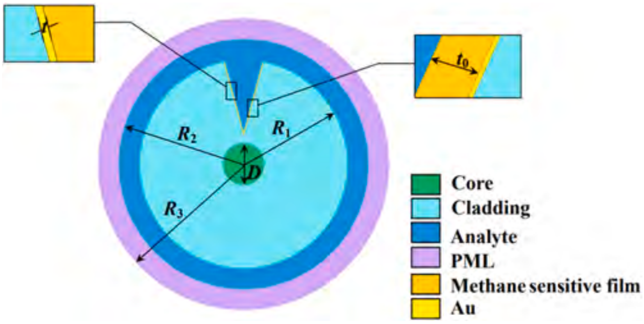

Fig. 1. Cross-section of the SMF-SPR sensor.

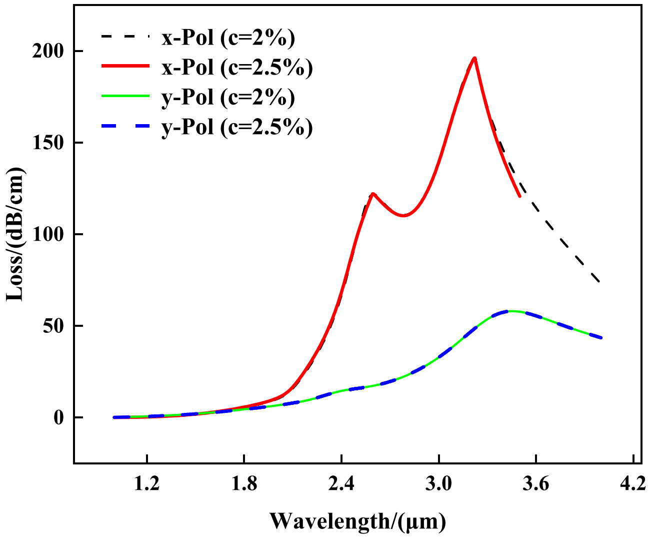

Fig. 2. x-pol and y-pol of c for 2 % and 2.5 %.

where λ is the wavelength and Im(n_{eff}) is the imaginary part of the effective refractive indexes. In order to achieve methane detection utilizing the SMF, a dual-resonance SMF-SPR sensor with a V-groove is designed (Fig. 1). The SMF consists of a core and cladding with the V-groove on the cladding. The inner side of the V-groove is coated with a gold film, and the outer side is coated with a gas-sensitive film. The light blue area in the figure is the cladding made of silicon dioxide, and its refractive index (RI) is obtained by the Sellmeier equation expressed in Eq. (4) [25]:

$$n^2(\lambda) = 1 + \frac{A_1\lambda^2}{\lambda^2 - B_1} + \frac{A_2\lambda^2}{\lambda^2 - B_2} + \frac{A_3\lambda^2}{\lambda^2 - B_3} \tag{4}$$

where $A_1 = 0.6961663$, $A_2 = 0.4079426$, $A_3 = 0.897479$, $B_1 = 0.0684043$, $B_2 = 0.1162414$, and $B_3 = 9.896161$. The green area is the core of the SMF-SPR sensor and RI is determined by Eq. (5) [26]:

$$n_{\mathrm{d}} = (100/99) \times n_{\mathrm{s}} \tag{5}$$

where n_{s} is the refractive index of silicon dioxide. The yellow area is coated with a gold film for excitation of SPR and the dielectric constant of gold is calculated by Eq. (6) [27]:

$$\varepsilon_{\mathrm{Au}}(\varepsilon) = \varepsilon_{\infty} - \frac{\omega_{\mathrm{p}}^2}{\omega(\omega + i\omega_{\tau})} \tag{6}$$

Where $\varepsilon_{\infty} = 9.75$, $\omega_{\mathrm{p}} = 1.36 \times 10^{16}$ rad/s, and $\omega_{\tau} = 1.45 \times 10^{14}$ rad/s. The orange area is the gas-sensitive film, which was derived from the experiment[39]. The linear relationship between the refractive index of the films and the methane concentration was obtained by extensive tests in the experiments, and its RI given by Eq. (7) [28]:

$$n\text{=}1.4478\text{–}0\cdot.38c, \tag{7}$$

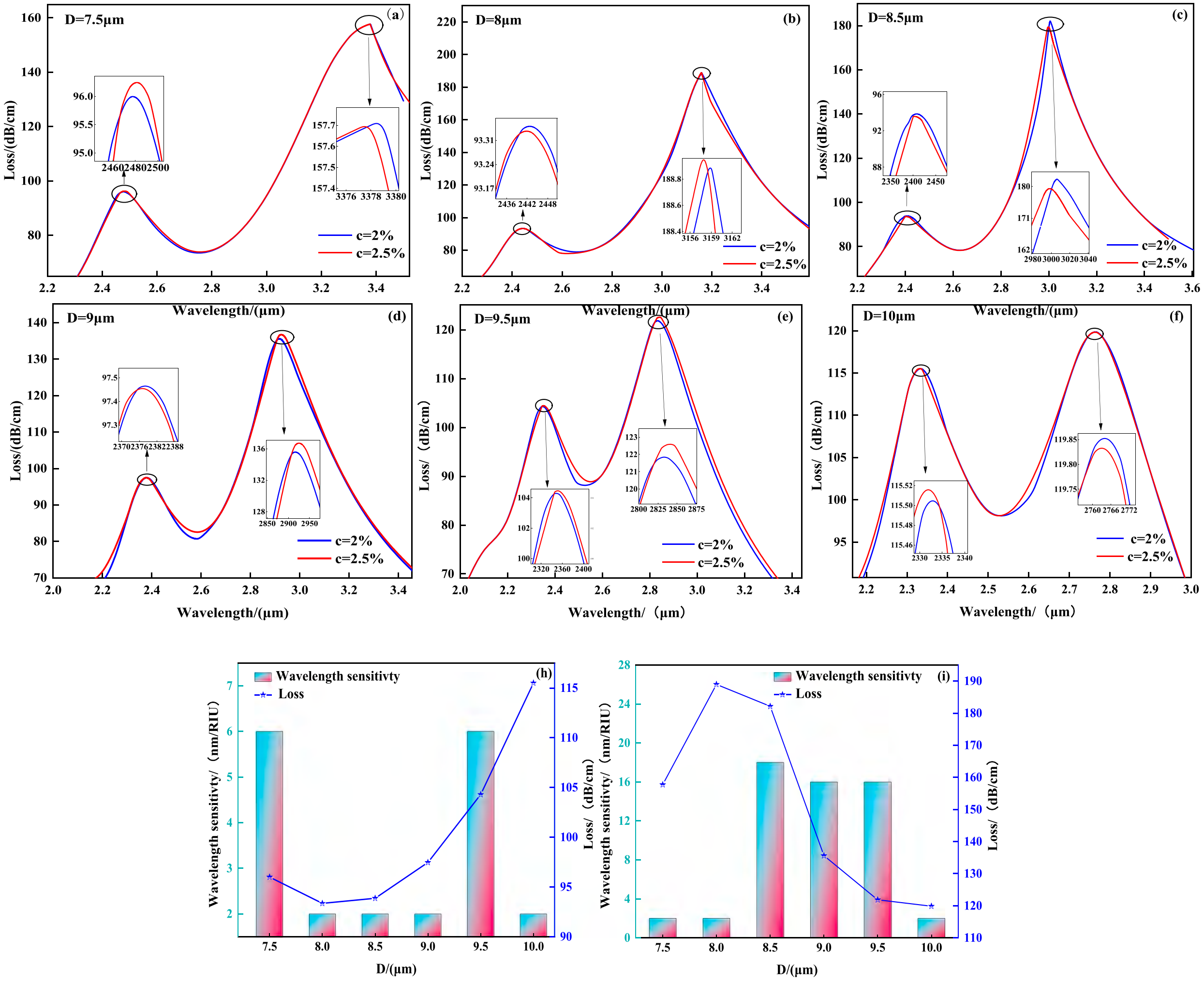

Fig. 3. (a) - (f) CL curves of the SMF-SPR sensors with different core D; CL and sensitivity: (h) First and (i) Second resonance peaks.

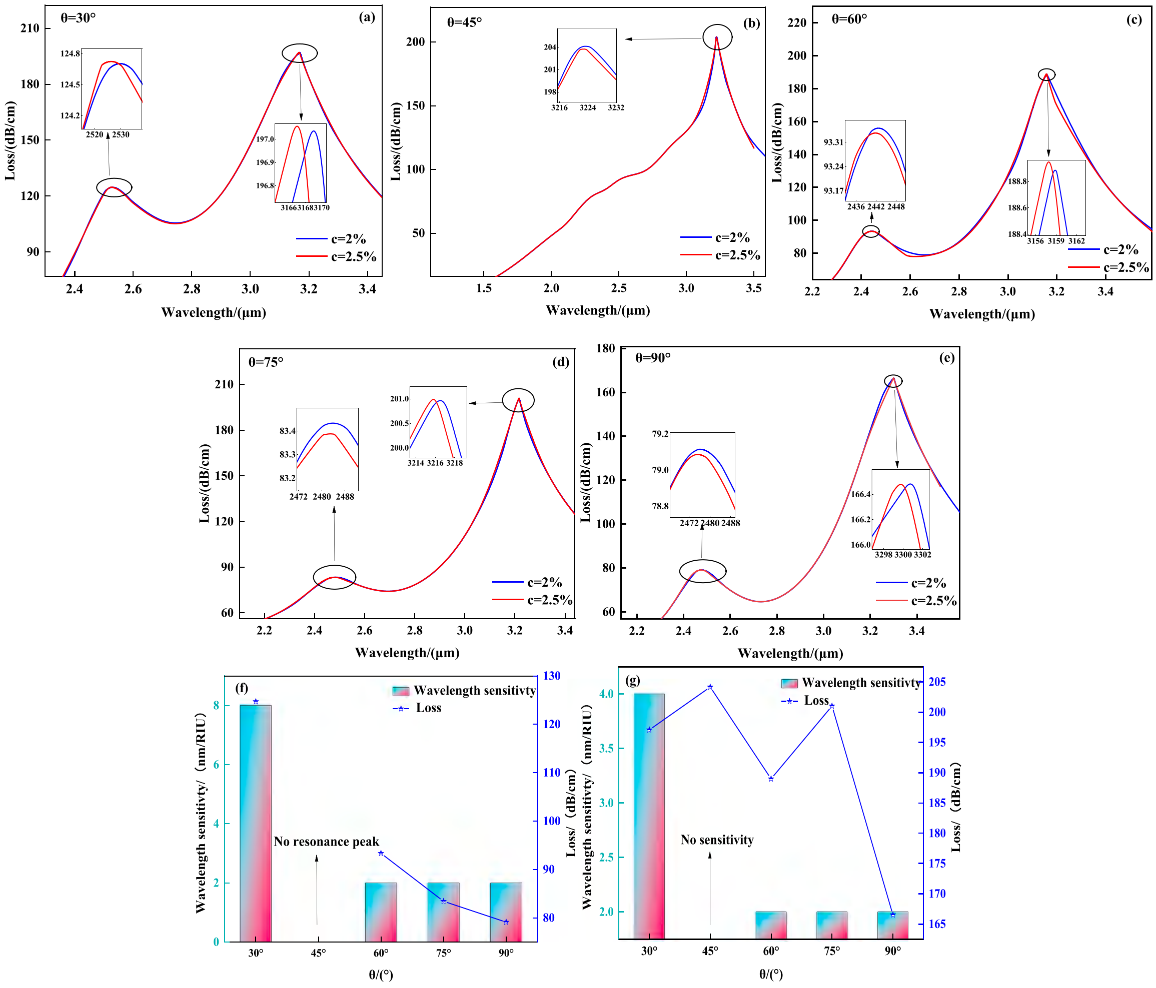

Fig. 4. (a) - (e) CL curves of the SMF-SPR sensors for different V-groove angles; CL and sensitivity: (f) First and (g) Second resonance peaks.

where c is the methane concentration, the film RI (n) decreases linearly with increasing methane concentration (c), which occurs due to the complexation reaction between cryptane A and methane molecules (cryptane A as the acceptor and methane molecules as the donor) in the induction film, resulting in a change in the dipole moment of cryptane A and the film RI. The dark blue area represents methane to be measured in the concentration range of 0–3.5 %, while the purple area is the perfect matching layer (PML) designed to provide the boundary conditions to limit radiation [19]. After several rounds of simulation using the finite element analysis software COMSOL [29], the initial parameters suitable for structural optimization are determined as follows: $D = 10.0$ μm, $\theta = 60°$, $t = 20$ nm, and $t_0 = 250$ nm, where D is the core diameter, t is the gold film thickness, t_0 is the gas sensitive film thickness, R_1 is the cladding radius, R_2 is the radius of the gas to be measured, and R_3 is the perfect match layer radius.

In order to obtain better sensing characteristics, it is important to choose the polarization direction of the fundamental mode. Based on the initial parameters, there are two mutually orthogonal polarization directions for the fundamental mode, i.e., x-pol and y-pol. Fig. 2 displays the CL spectra in the two polarization directions for gas concentrations of 2 % and 2.5 %, revealing that x-pol has two resonance peaks with the second one being much higher and y-pol only has a second resonance peak. As the wavelength red-shifts, the CL of both resonance peaks of x-pol increases first and then decreases, and the second resonance peak of y-pol exhibits a similar trend. The two resonance peaks of x-pol are significantly stronger than those of y-pol, indicating that x-pol has a larger evanescent field and stronger coupling effects with the gold film.

Hence, x-pol is selected for subsequent structural optimization of the core diameter, V-groove angle, gold film thickness, and gas-sensitive film thickness. Using the wavelength sensitivity as an optimization indicator, the ratio of the resonance wavelength difference of the adjacent gas concentration CL spectra to the difference in the adjacent gas concentration is shown in Eq. (8) [30]:

$$S_n = \frac{\Delta\lambda_{\text{peak}}}{\Delta c_a} \tag{8}$$

where $\Delta\lambda_{\text{peak}}$ is the resonance wavelength difference of adjacent gas concentration CL spectra and Δc_a is the concentration difference of

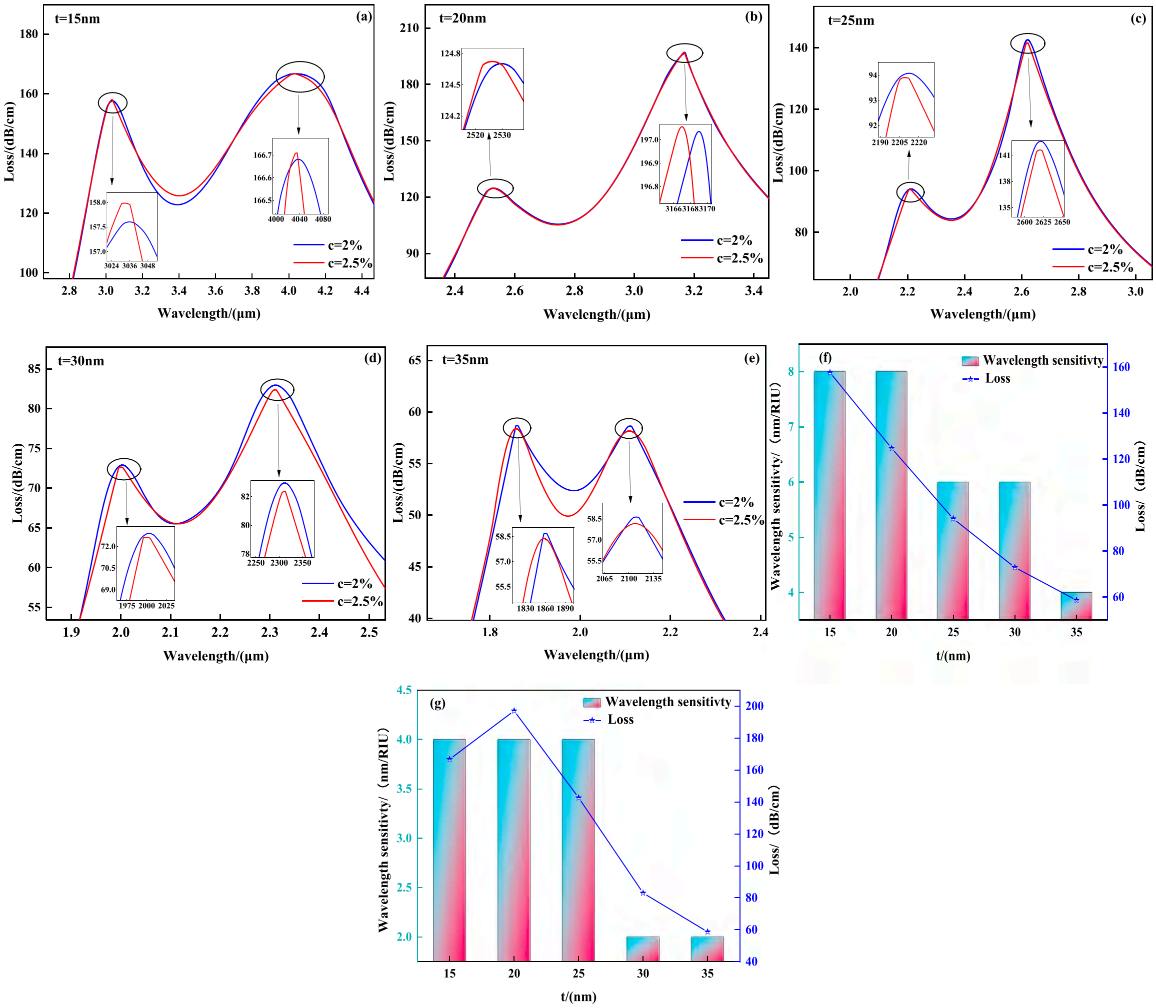

Fig. 5. (a) - (e) CL curves of SMF-SPR sensors for different gold film thicknesses; CL and sensitivity: (f) First and (g) Second resonance peaks.

adjacent gases.

In order to obtain the appropriate initial parameter values, a large number of rough simulation calculations are carried out, which ensures that the designed sensor can transmit mode stably and achieve the SPR effect. In addition, the extent to which each parameter affects the sensor performance is demonstrated in the process, and several important parameters will be further optimized for better performance. Based on the original parameters of the SMF, optimization is performed for core *D* between 7.5 μm and 10 μm. The optimization process is demonstrated in Fig. 3, in which (a) - (f) are the loss curves of methane for different core *D* and methane concentrations of 2 % and 2.5 %, and Fig. 3(h) and (i) present the wavelength sensitivity and CL of the first and second resonance peaks for different core *D*.

The resonance wavelengths of both resonance peaks blue-shift with increasing core *D*. As *D* increases, the first resonant peak of the fundamental mode CL decreases first and then increases, and the CL reaches the lowest at $D = 8$ μm, indicating that photon energy can be effectively confined to the core to reduce the energy transfer to the SPP mode on the gold film. It is emphasized that optimization of core *D* is important, as it affects the position and intensity of the resonance peaks and the detection sensitivity. The second resonance peak exhibits an opposite tendency. With increasing D, the second resonance peak guide mode CL increases initially and then diminishes. At $D = 8$ μm, the second resonance peak is intense and sharp, and the CL peak reaches the maximum, suggesting that the core energy is coupled to the SPP mode to excite SPR and increase the CL value and sensitivity of the guide mode. Therefore, *D* is chosen to be 8 μm.

The V-groove angle is then optimized between 30° and 90°, and the resonant wavelength and CL curves are presented in Fig. 3(a) - (e) for different θ. The results of θ optimization are summarized in Fig. 3(f) and (g) [19].

Fig. 4(a) - (e) show that when θ is 45°, the SPR is difficult to excite. The first resonance peak disappears, and only the second resonance peak can be used for sensing. However, the sensitivity of the second resonance peak is quite low and almost negligible. When θ is changed from this value, both show two resonance peaks, and when θ is 30°, the wavelength sensitivity is the highest for gas

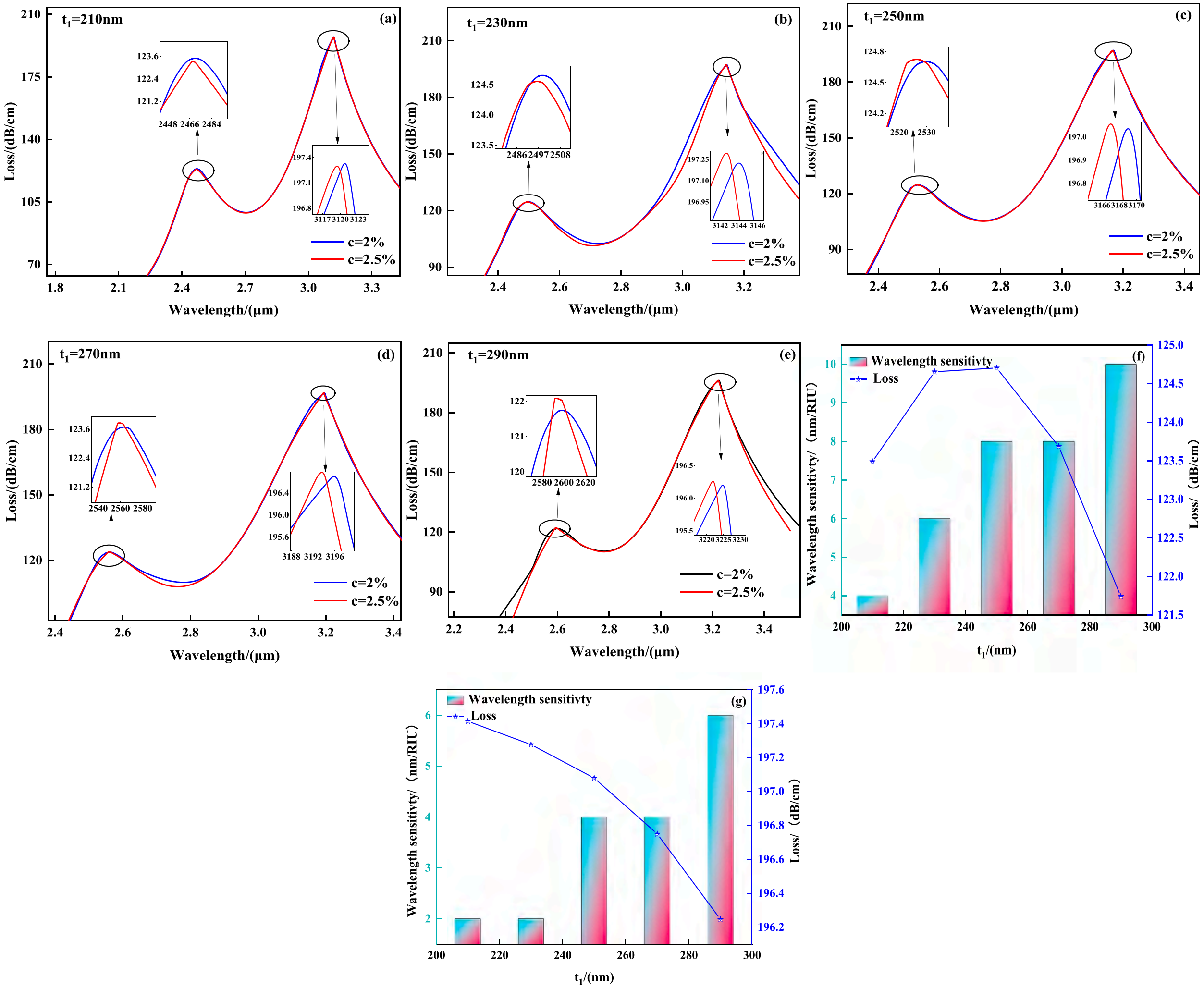

Fig. 6. (a) - (e) CL curves of SMF-SPR sensors for different gas-sensitive film thicknesses; CL and sensitivity: (f) First and (g) Second resonance peaks.

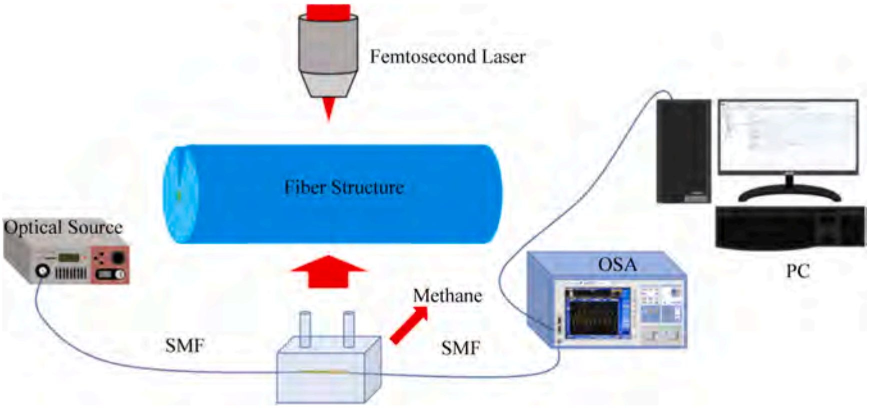

Fig. 7. Schematic of the SMF-SPR sensor.

concentrations of 2 % and 2.5 %. According to Fig. 4(f) and (g), the wavelength sensitivity of the two resonance peaks is almost constant when θ is larger than 45°, indicating that the real part of the effective refractive index (Re(n_{eff})) of the fundamental mode and SPP mode hardly changes with increasing angle. Therefore, there is almost no effect on the sensitivity of the sensor and the optimal angle θ is 30°.

The V-groove is coated with a gold film and gas-sensitive film, and the thicknesses of the gold film and gas-sensitive film are the major parameters affecting the sensing efficiency. In the structural optimization, the inside-out sequence is adopted and the gold film thickness is optimized first. The CL curves shown in Fig. 5 are derived for 15 nm $< t <$ 35 nm.

As the thickness of the gold film increases, the resonance wavelengths of both resonance peaks shift to shorter wavelengths mainly due to the decrease of Re(n_{eff}) of the SPP mode, but Re(n_{eff}) of the fundamental mode does not change obviously. The phase matching point (resonance wavelength) of the SPP mode and the fundamental mode move to shorter wavelengths. The relationship between the fundamental mode CL of the first and second resonance peaks and resonance wavelength is shown in Fig. 5(f) and (g). When t is varied from 15 nm to 35 nm, the CL peak intensities of the first and second resonance peaks decrease with increasing gold film thickness, and the highest wavelength sensitivity is obtained at a gas concentration of 2 % when the gold film thickness is 15 nm or 20 nm. This is mainly because if the gold film is too thick, the electromagnetic wave cannot easily penetrate the gold film, and coupling between the fundamental mode and SPP mode weakens so that SPR cannot be excited fully. When the thickness of the gold film is 15 nm, the second resonance peak resonance wavelength is 4038 nm. Since the requirements of the light source are quite stringent, the thickness of the gold film is selected to be 20 nm.

The thickness t_0 of the gas-sensitive film is then optimized. Fig. 6(a) - (e) show that for 210 nm $< t_0 <$ 290 nm, the resonance wavelengths of both resonance peaks move to longer wavelengths with increasing gas-sensing film thickness. The thickness of the gas-sensitive film is smaller than the penetration depth of the evanescent waves, and a significant portion of the light energy penetrates the gas-sensitive film and propagates in the nearby air, making the effective refractive index (RI) of the SPP mode on the surface of the metal film to increase thus producing a red-shift in the resonant wavelength. Fig. 6(f) and (g) show that the overall CL of the two resonance peaks decreases as the thickness of the gas-sensitive film increases, and the wavelength sensitivity peaks at a gas concentration of 2 % when the gas-sensitive film is 290 nm thick. Hence, the optimal t_0 is 290 nm, and the maximum wavelength sensitivity of the two resonance peaks is 10 nm/% and 6 nm/%, respectively.

In summary, the optimal parameters of the SMF-SPR sensor are: $D = 8.0$ μm, $\theta = 30°$, $t = 20$ nm, and $t_0 = 290$ nm.

After theoretically optimizing the structural parameters of SMF, the manufacturing complexity and difficulty are analyzed. Owing to the mature manufacturing technology of SMF, production of the structure can be carried out using femtosecond technology to polish the V-groove after manufacturing by wire drawing tower. Controlling the polishing time and pulse frequency, multiple treatments are performed to focus the laser to a certain distance from the beam waist into the molten silicon substrate, thus realizing a three-dimensional scanning of the surface and interior of the transparent silicon substrate by the laser focus. It is worth mentioning that here the laser only changes the physical properties of the material and has no significant effect on the performance of the sensor [31]. For the gold film, magnetron sputtering technique is used to get the thickness of the gold film we want by controlling the deposition conditions such as sputtering time, power and pressure. In order to obtain a uniform gas-sensitive film on the surface of the V-groove, the filling of the gas-sensitive film can be achieved using chemical vapor deposition (CVD) technology to provide minimal surface roughness [32]. The SMF is placed in the gas environment utilizing a fiber fusion machine to connect the SMF on both sides of the sensor, with one end connected to a light source and the other end connected to an optical spectrum analyzer (OSA). A data cable connects the OSA to the PC [19]. After turning on the light source and adjusting the appropriate wavelength, the CL curve is obtained on the OSA to determine the corresponding resonance wavelength. The detection process of the SMF-SPR sensor is illustrated in Fig. 7 [33]. The unique CL curves for different methane concentrations mean that each methane concentration corresponds to a single resonance wavelength, and the methane concentration can be determined by calculating the resonance wavelength.

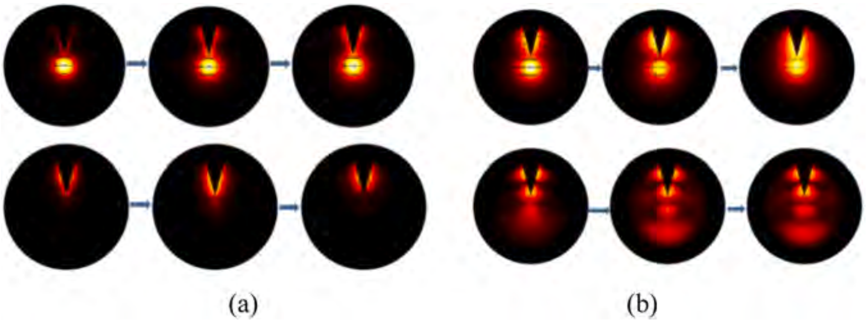

Fig. 8. Electric field distributions: (a) First resonance peak and (b) Second resonance peak of the fundamental mode and SPP mode.

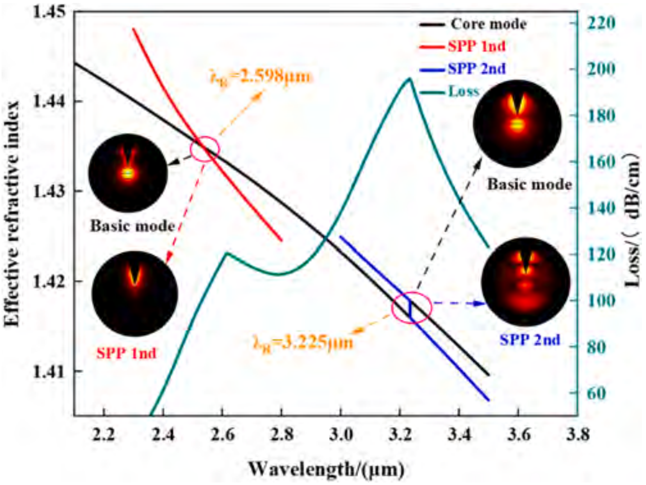

Fig. 9. Relationship between the SPP mode, guided mode, and CL with wavelength.

3. Results and discussion

3.1. Coupling properties

The essence of SPR is the energy exchange between the fundamental mode and the metal plasmonic mode, and so the light field distributions of these two modes are employed to explain the SPR phenomenon. Figs. 8(a) and 8(b) depict the field distributions of the two resonance peaks near the resonance wavelength for the fundamental mode and SPP mode. Both resonance peaks exhibit the same trend. Before reaching the resonance wavelength, most of the energy of the incident light is concentrated in the core. Very little energy is near the metal film, indicating that little energy transfer occurs between the fundamental mode and SPP mode [29]. When the propagation constants of the evanescent waves and SPW are equal, most of the energy of the incident light is converted into the energy of SPW, indicating strong coupling between the fundamental mode and SPP mode to excite SPR. After reaching the resonance wavelength, Re(n_{eff}) of the fundamental mode is larger than that of the SPP mode, at which time the photon energy moves back to the core from near the metal film, and the energy in the fundamental mode is higher than that of the SPP mode [27].

Fig. 9 shows the variations of the SPP mode, guide mode, and CL with wavelength, and (Re(n_{eff})) of the guided mode, SPP first-order mode, and second-order mode is shown as black, red, and blue lines respectively [34]. As the wavelength increases, Re(n_{eff}) of the three modes decline at different rates, but they all show the same Re(n_{eff}) at 2598 nm and 3225 nm. The relationship between the CL and wavelength represented by the green line shows that the maximum CL peak of the first resonance peak occurs at the junction of the black and red lines, and the maximum CL peak of the second resonance peak is at the intersection of the black and blue lines. Hence, both the first and second resonance peaks meet the phase-matching conditions for the generation of SPR.

3.2. Gas sensing

Fig. 10 shows the relationship between the resonance wavelength and CL for different gas concentrations, revealing that the CL of the two resonance peaks is positively correlated with the gas concentration and that of the second resonance peak is significantly greater than that of the first resonance peak. Regarding the first resonance peak, before the wavelength of 2662 nm, the CL increases

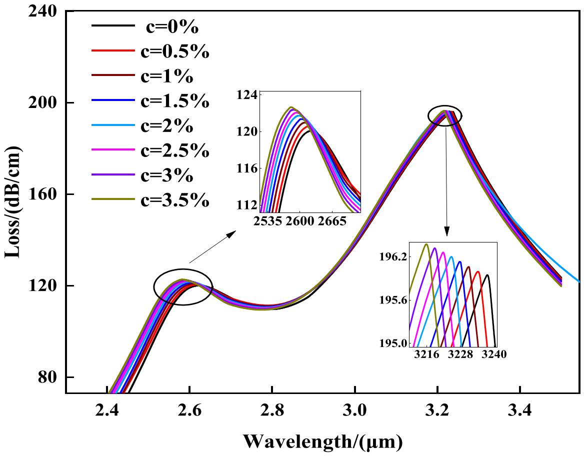

Fig. 10. Relationship between the resonance wavelength and CL for different gas concentrations.

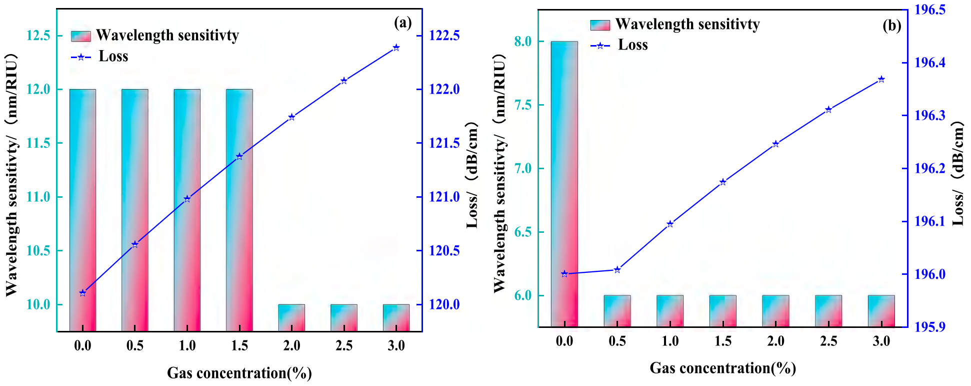

Fig. 11. Wavelength sensitivity and CL: (a) First and (b) Second resonance peaks for the gas concentration range of 0–3 %.

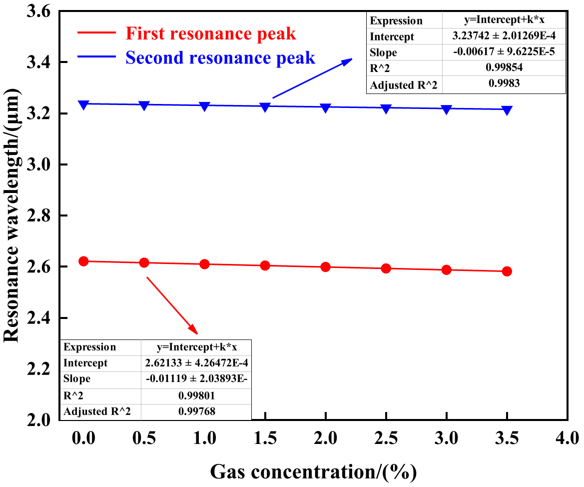

Expression	y=Intercept+k*x
Intercept	3.23742 ± 2.01269E-4
Slope	-0.00617 ± 9.6225E-5
R^2	0.99854
Adjusted R^2	0.9983

Expression	y=Intercept+k*x
Intercept	2.62133 ± 4.26472E-4
Slope	-0.01119 ± 2.03893E-
R^2	0.99801
Adjusted R^2	0.99768

Fig. 12. Fitted linear relationship between the resonance wavelength and gas concentration.

gradually with gas concentration but between 2662 nm and 2900 nm, it decreases. The second resonance peak also shows the same variation, and the resonance wavelengths of both resonance peaks blue-shift with gas concentrations.

The wavelength sensitivity is defined as the ratio of the resonance wavelength difference of the adjacent gas concentration CL

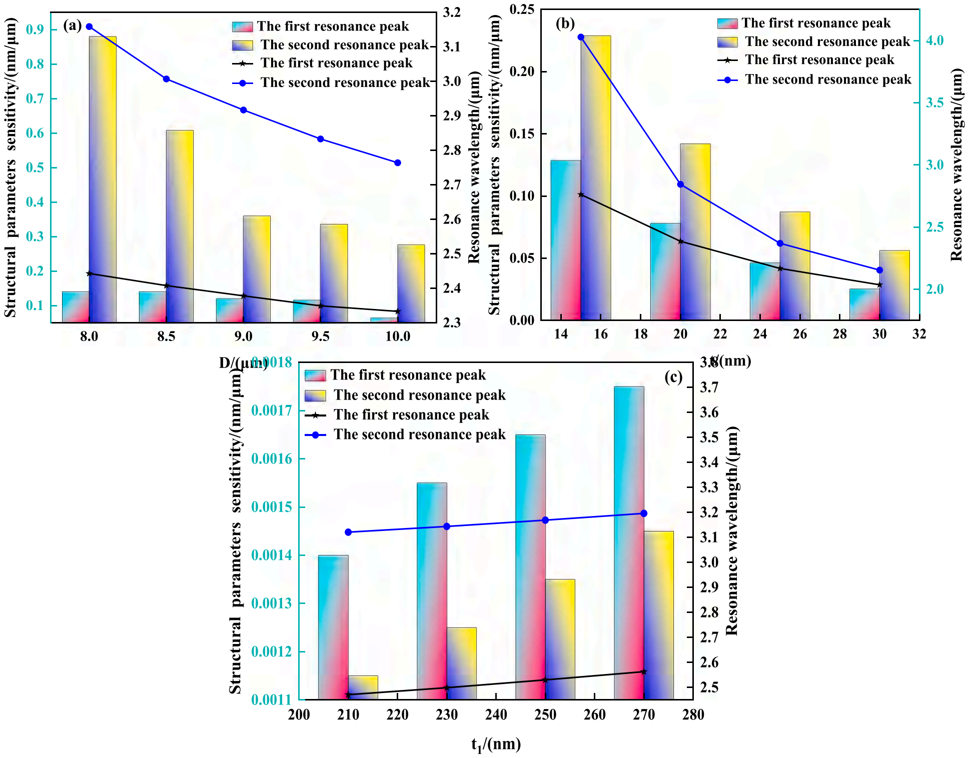

Fig. 13. Sensitivity curves of the structural parameters: (a) Core diameter, (b) Gold film thickness, (c) Gas-sensitive film thickness for a gas concentration of 2 %.

spectra to the difference in the adjacent gas concentration, as shown in Eq. (8). Fig. 11(a) and (b) summarize the wavelength sensitivity and CL of the first and second resonance peaks for the gas in Fig. 10 in the 0–3 % concentration range. The maximum wavelength sensitivity of the first resonance peak is 12 nm/% and the average wavelength sensitivity is 11.14 nm/%. The maximum wavelength sensitivity of the second resonance peak is 8 nm/% and the average wavelength sensitivity is 6.29 nm/%. The results indicate desirable sensing characteristics with those of the first resonance peak being better than those of the second resonance peak.

By linearly fitting the resonance wavelength relationship in Fig. 10, the expression between the resonance wavelengths corresponding to different gas concentrations and CL peaks can be derived from Fig. 11 and expressed in Eqs. (9) and (10) [19]:

$$\lambda_1 = 2.62 - 0.0112c, 0 \leq c \leq 3.5 \tag{9}$$

and

$$\lambda_2 = 3.24 - 0.00617c, 0 \leq c \leq 3.5 \tag{10}$$

where λ_1 and λ_2 are the resonance wavelengths of the first and second resonance peaks, respectively, and c is the methane concentration. The fitted curves in Fig. 12 show that the R_2 values of the first and second resonance peaks are 99.801 % and 99.854 %, respectively, confirming good linearity.

Another important parameter is the resolution which refers to the ability to detect minimal changes in weak signals. According to Eq. (11) [35],

$$R_n = \frac{\Delta n_a \Delta\lambda_{\min}}{\Delta\lambda_{peak}} = \frac{\Delta\lambda_{\min}}{S_n} \tag{11}$$

where S_n is the wavelength sensitivity and Δλmin is the minimum measured value by the spectral analyzer (OSA) usually related to the instrument. Under the present conditions, $\Delta\lambda_{\min} = 0.2$ nm, and the resolution of the two resonance peaks is positively correlated with the gas concentration. The minimum resolution of the first resonance peak is 0.0166 % and the average resolution is 0.018 %, while the minimum resolution of the second resonance peak is 0.026 % and the average resolution is 0.032 %. The resolution of the first resonance peak is lower than that of the second resonance peak due to the high wavelength sensitivity of the first resonance peak. Therefore, its ability to detect weak signal changes is better than that of the second resonance peak.

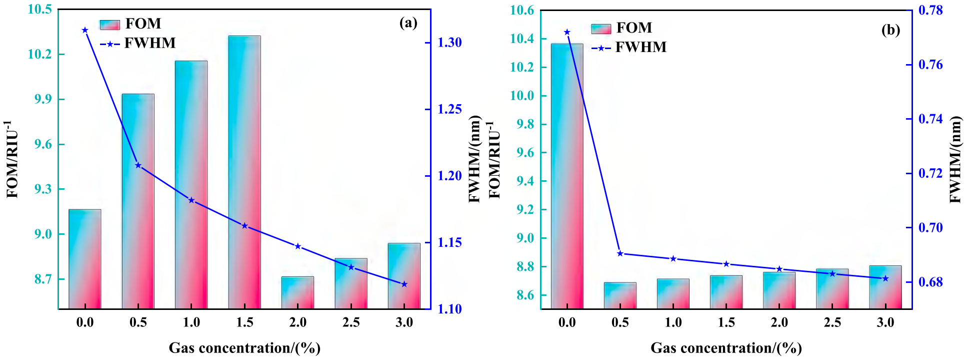

Fig. 14. Figures of merit (FOM) and full-width at half-maximum (FWHM) of the (a) first and (b) second resonance peaks for different gas concentrations.

3.3. Structural parameter sensitivity

In commercial production, tolerance must be allowed for the designed parameters and features to allow for manufacturing errors that can affect the properties of the products. The structural parameters sensitivity, which reflects the effects of the changes in the optical fiber parameters on the resonance wavelength, is defined as the ratio of the change in the resonance wavelength to the change in the structural parameters [36]. Fig. 13(a), (b), and (c) plot the structural parameter sensitivity curves for the core diameter, gold film thickness, and gas-sensitive film thickness for a gas concentration of 2 %.

Changing these parameters affects the overall structural sensitivity. With regard to the core diameter, the sensitivity of the first resonance peak structural parameter is significantly lower than that of the second resonance peak, and the sensitivity of the structural parameters of the first resonance peak shows a minimum of 0.064 nm/μm. As for the gold film, the sensitivity of the structural parameters of the first and second resonance peaks decreases with gold film thickness. The sensitivity of the structural parameters of the two resonance peaks is the smallest when the gold film is 30 nm thick, namely 0.0286 nm/μm and 0.0404 nm/μm, respectively. Regarding the gas-sensitive film, the trend of the two resonance peaks is opposite to that of the gold film. The sensitivity of the two resonance peak structural parameters is the lowest when the gas-sensitive film is 210 nm thick, which is 0.0014 nm/μm and 0.00115 nm/μm, respectively. By calculating the three parameters, the core diameter has the highest structural parameter sensitivity, indicating that the core diameter will have a greater impact on the SMF-SPR performance. Consequently, in actual manufacturing, the core diameter should be considered carefully.

3.4. Figure of merit (FOM)

Wavelength sensitivity is an important parameter to measure the performance of the sensor, but FOM is a comprehensive measure of sensor performance. It is defined as the ratio of the wavelength sensitivity to full-width at half-maximum by Eq. (12) [37]:

$$FOM = \frac{S_n}{FWHM} \tag{12}$$

where S_n is the wavelength sensitivity and the full-width at half-maximum (FWHM) refers to the frequency band corresponding to half the height of the CL peak. Fig. 14(a) and (b) present the FOM and FWHM of the first and second resonance peaks for different concentrations. We are mainly describing the relationship between FOM and gas concentration, while FWHM is only an intermediate parameter for calculating FOM. So the slope just describes the direction of this relationship with concentration, which has little practical significance.

The first resonance peak increases initially, decreases, and then increases with increasing gas concentration. The maximum FOM is 10.32 % at a concentration of 1.5 %. The second resonance peak exhibits the same trend as the gas concentration increases. When the gas concentration is 0 %, the maximum FOM is 10.36 %, indicating good characteristics for both resonance peaks.

3.5. Signal-to-noise ratio (SNR)

The signal-to-noise ratio (SNR) is defined as the ratio of the resonant wavelength difference of adjacent gas concentrations to the full-width at half-maximum (FWHM) as shown in Eq. (13) [38]:

$$SNR = \frac{\Delta\lambda_R}{FWHM} \tag{13}$$

where $\Delta\lambda_R$ is the adjacent gas concentration resonance wavelength difference. Fig. 15 reveals the SNR of the first resonance peak and second resonance peak for different gas concentrations. The trend follows that of the FOM, and the SNR of the first resonance peak at a concentration of 1.5 % and the second resonance peak at a concentration of 0 % are maximum at 0.00516 and 0.00518, respectively.

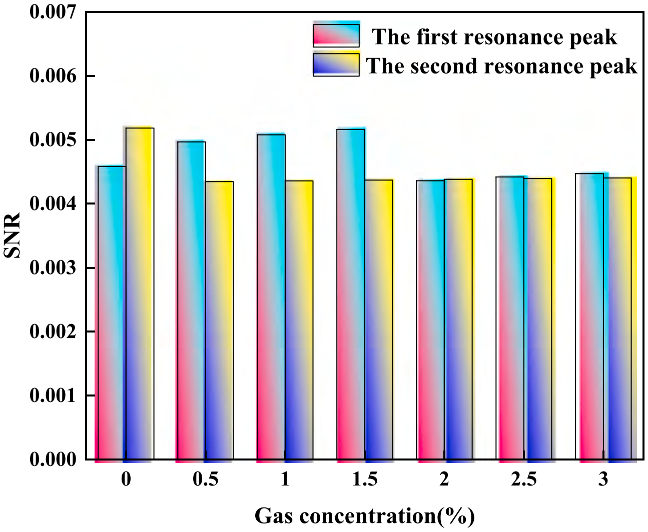

Fig. 15. SNR of the first resonance peak and second resonance peak for different gas concentrations.

Table 1
Comparison of the properties of different sensors.

Ref.	Fiber structure	Methane Sensitive film	Detection Range (%)	WS / (nm/%)	Detection Limit (ppm)	Str. diagram
[39]	HC-ARF; SPR	Cryptophane A	0–3.5	5.54	-	
[40]	Four ultralarge sideholes; PCF-SPR	Cryptophane A	0–3.5	1.99	1005 (Δλmin = 0.2 nm)	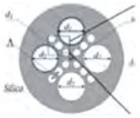
[14]	PCF-LPG	CryptophaneA-6Me	0–3.5	1.078	1800 (Δλmin = 0.2 nm)	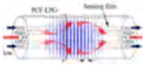
[12]	Solid PCF; Modal interference	Cryptophane A	0–3.5	0.514	1600 (Δλmin = 0.2 nm)	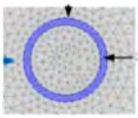
This work	V-Groove SMF SPR	Au	0–3.5	12	166 (Δλmin = 0.2 nm)	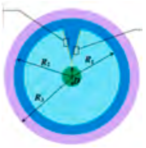

The first resonance peak at a concentration of 1.5 % and the second resonance peak at a concentration of 0 % deliver the best sensing performance. Table 1 compares the optical properties of recently studied methane sensors. The structural design contributes decisively to the performance of the sensors. A range of characteristics are listed in the table for comparison. The sensor is not only simple in structure but also more sensitive compared to the previous proposed sensor. Hence, the proposed sensor will present great potential in the field of life safety.

4. Conclusion

A dual resonant-peak SMF-SPR gas sensor with a V-groove is developed for methane detection. The unique V-groove and composite coating boost the sensing performance. By performing systematic and comprehensive parameter optimization, the figure of merit, signalto-noise ratio, and other parameters are determined and analyzed. The Numerical simulations show that the resolution is less than 0.017, minimum structural sensitivity is 0.0014 nm/μm, wavelength sensitivity is more than 6 nm/%, and at a methane concentration of 0 %, the maximum FOM and SNR are 10.36 % and 0.0052. Owing to the simple design and remarkable sensing characteristics, the SMF-SPR sensor has large commercial potential in the detection of flammable and explosive gases.

Declaration of Competing Interest

The authors declare no conflicts of interest.

Data availability

The authors do not have permission to share data.

Acknowledgements

This work was jointly supported by Heilongjiang Provincial Natural Science Foundation of China [JQ2023F001], Outstanding Young and Middle-aged Research and Innovation Team of Northeast Petroleum University [KYCXTD201801], Local Universities Reformation and Development Personnel Training Supporting Project from Central Authorities, Postdoctoral Scientific Research Development fund of Heilongjiang Province (LBH-Q20081), City University of Hong Kong Donation Research Grant [DON-RMG No. 9229021], City University of Hong Kong Strategic Research Grant [SRG 7005505], and City University of Hong Kong Donation Grant [9220061].

References

[1] Y. Zhang, Y. Zhao, Q. Wang, Measurement of methane concentration with cryptophane E infiltrated photonic crystal microcavity, Sens. Actuators B Chem. 209 (2015) 431–437.
[2] H. Nazemi, A. Joseph, J. Park, Advanced micro-and nano-gas sensor technology: a review, Sensors 19 (6) (2019) 1285.
[3] F. Wu, P. Shi, Z. Yi, et al., Ultra-broadband solar absorber and high-efficiency thermal emitter from uv to mid-infrared spectrum, Micromachines 14 (5) (2023) 985.
[4] Q. Li, J. Wang, H. Mu, A Fabry–Pérot interferometer strain sensor composed of a rounded rectangular air cavity with a thin wall for high sensitivity and interference contrast, Opt. Commun. 527 (2023), 128920.
[5] J.K. Sahota, N. Gupta, D. hawan, Fiber Bragg grating sensors for monitoring of physical parameters: a comprehensive review, Opt. Eng. 59 (6) (2020), 060901.
[6] S.N. Meitei, K. Borah, S. Chatterjee, Partial discharge detection in an oil-filled power transformer using fiber Bragg grating sensors: a review, IEEE Sens. J. 21 (9) (2021) 10304–10316.
[7] J.C. Lecullier, G. Chanin, A scanning Fabry-Perot interferometer for the 50–1000 μm range, Infrared Phys. 16 (1–2) (1976) 273–278.
[8] R. Lai, P. Shi, Z. Yi, et al., Triple-band surface plasmon resonance metamaterial absorber based on open-ended prohibited sign type monolayer graphene, Micromachines 14 (5) (2023) 953.
[9] Y. Zheng, Z. Yi, L. Liu, et al., Numerical simulation of efficient solar absorbers and thermal emitters based on multilayer nanodisk arrays, Appl. Therm. Eng. 230 (2023), 120841.
[10] Y. Zhu, P. Cai, W. Zhang, et al., Ultra-wideband high-efficiency solar absorber and thermal emitter based on semiconductor InAs microstructures, Micromachines 14 (8) (2023) 1597.
[11] R. Lai, P. Shi, Z. Yi, et al., Triple-band surface plasmon resonance metamaterial absorber based on open-ended prohibited sign type monolayer graphene, Micromachines 14 (5) (2023) 953.
[12] H. Liu, M. Wang, Q. Wang, Simultaneous measurement of hydrogen and methane based on PCF-SPR structure with compound film-coated side-holes, Opt. Fiber Technol. 45 (2018) 1–7.
[13] J. Yang, X. Che, R. Shen, High-sensitivity photonic crystal fiber long-period grating methane sensor with cryptophane-A-6Me absorbed on a PAA-CNTs/PAH nanofilm, Opt. Express 25 (17) (2017) 20258–20267.
[14] Y. Zhang, Y. Zhao, Q. Wang, Measurement of methane concentration with cryptophane E infiltrated photonic crystal microcavity, Sens. Actuators B Chem. 209 (2015) 431–437.
[15] Q. Wu, Y. Semenova, B. Yan, Fiber refractometer based on a fiber Bragg grating and single-mode–multimode–single-mode fiber structure, Opt. Lett. 36 (12) (2011) 2197–2199.
[16] F.F. Sabins, Remote sensing for mineral exploration, Ore Geol. Rev. 14 (3–4) (1999) 157–183.
[17] Y. Yang, Z. Yuan, R. Meng, Exploring traffic crash occurrence mechanism toward cross-area freeways via an improved data mining approach, J. Transp. Eng., Part A Syst. 148 (9) (2022), 04022052.
[18] J. Lv, H. Fu, C. Liu, Double-formant surface plasmon resonance for refractive index sensing by anti-resonance fibers with high sensitivity and wide detection range, Results Phys. 40 (2022), 105876.
[19] Z. Chen, P. Cai, Q. Wen, et al., Graphene multi-frequency broadband and ultra-broadband terahertz absorber based on surface plasmon resonance, Electronics 12 (12) (2023) 2655.
[20] D. Yang, H.H. Lu, B. Chen, Surface plasmon resonance of SnO2/Au Bi-layer films for gas sensing applications, Sens. Actuators B Chem. 145 (2) (2010) 832–838.
[21] P. Zhang, Y. Xiao, J. Zhang, Highly sensitive gas sensing platforms based on field effect transistor-a review, Anal. Chim. Acta 1172 (2021), 338575.
[22] J. Yang, L. Zhou, X. Che, et al., Photonic crystal fiber methane sensor based on modal interference with an ultraviolet curable fluoro-siloxane nano-film incorporating cryptophane A, Sens. Actuators B Chem. 235 (2016) 717–722.
[23] W. Liu, Z. Yi, C. Liu, Surface plasmon resonance sensor composed of microstructured optical fibers for monitoring of external and internal environments in biological and environmental sensing, Results. Phys. 47 (2023) 106365.
[24] Y. Xu, X. Chen, Y. Zhu, High sensitive temperature sensor using a liquid-core optical fiber with small refractive index difference between core and cladding materials, Sensors 8 (3) (2008) 1872–1878.
[25] W. Liu, C.J. Liu, A square-lattice D-shaped photonic crystal fiber sensor based on SPR to detect analytes with large refractive indexes, Phys. E. 138 (2022) 115106.
[26] H. Liu, H. Wang, C. Chen, High sensitive methane sensor based on twin-core photonic crystal fiber with compound film-coated side-holes, Opt. Quantum Electron. 52 (2020) 1–10.
[27] L. Xu, C. Liu, H. Fu, Orbital angular momentum-excited surface plasmon resonance for liquid refractive index sensing by photonic crystal fiber with high sensitivity and wide detection range, Opt. Eng. 61 (9) (2022), 096101.

[28] M.R. Islam, M.A. Jamil, S.A.H. Ahsan, Highly birefringent gold-coated SPR sensor with extremely enhanced amplitude and wavelength sensitivity, Eur. Phys. J. 136 (2) (2021), 238.
[29] T. Aldhafeeri, M.K. Tran, R. Vrolyk, A review of methane gas detection sensors: recent developments and future perspectives, Inventions 5 (3) (2020) 28.
[30] W. Liu, Y. Shi, Z. Yi, Surface plasmon resonance chemical sensor composed of a microstructured optical fiber for the detection of an ultra-wide refractive index range and gas-liquid pollutants, Opt. Express 29 (25) (2021) 40734–40747.
[31] T. Yang, Y. Bellouard, Tunable 3D monolithic glass dielectrophoretic actuator for optomechanics, in: in: Proceedings of the Ninteenth International Conference on Solid-State Sensors, Actuators and Microsystems (TRANSDUCERS), 2017, IEEE, 2017, pp. 922–925.
[32] N. Sakib, W. Hassan, Q.M. Kamrunnahar, et al., Dual core four open channel circularly slotted gold coated plasmonic biosenso, Opt. Mater. Express 11 (2) (2021) 273–288.
[33] W. Huber, A new strategy for improved secondary screening and lead optimization using high-resolution SPR characterization of compound–target interactions, J. Mol. Recognit. Interdiscip. J. 18 (4) (2005) 273–281.
[34] T. Huang, Highly sensitive SPR sensor based on D-shaped photonic crystal fiber coated with indium tin oxide at near-infrared wavelength, Plasmonics 12 (2017) 583–588.
[35] R. Tabassum, B.D. Gupta, SPR based fiber-optic sensor with enhanced electric field intensity and figure of merit using different single and bimetallic configurations, Opt. Commun. 367 (2016) 23–34.
[36] A.K. Sharma, B.D. Gupta, Influence of temperature on the sensitivity and signal-to-noise ratio of a fiber-optic surface-plasmon resonance sensor, Appl. Opt. 45 (1) (2006) 151–161.
[37] T. Aldhafeeri, M.K. Tran, R. Vrolyk, A review of methane gas detection sensors: recent developments and future perspectives, Inventions 5 (3) (2020) 28.
[38] Y.X. Li, H.L. Chen, Q. Chen, Surface plasmon resonance induced methane gas sensor in hollow core anti-resonant fiber, Opt. Fiber Technol. 78 (2023), 103293.
[39] H. Liu, M. Wang, Q. Wang, Simultaneous measurement of hydrogen and methane based on PCF-SPR structure with compound film-coated side-holes, Opt. Fiber Technol. 45 (2018) 1–7.
[40] H. Liu, H.R. Wang, C.C. Chen, “High sensitive methane sensor based on twin-core photonic crystal fiber with compound film-coated side-holes, Opt. Quantum Electron. 52 (2020) 1–10.